# Surface Reengineering of RPA70N Enables Cocrystallization with an Inhibitor of the Replication Protein A Interaction Motif of ATR Interacting Protein

Michael D. Feldkamp,[†,∥] Andreas O. Frank,[†,∥,⊥] J. Phillip Kennedy,[§] James D. Patrone,[§] Bhavatarini Vangamudi,[†] Alex G. Waterson,[∥,‡] Stephen W. Fesik,[†,∥,§,‡] and Walter J. Chazin*,[†,∥,‡]

[†]Department of Biochemistry, [‡]Department of Chemistry, [§]Department of Pharmacology, and [∥]Center for Structural Biology, Vanderbilt University, Nashville, Tennessee 37232, United States

S *Supporting Information*

ABSTRACT: Replication protein A (RPA) is the primary single-stranded DNA (ssDNA) binding protein in eukaryotes. The N-terminal domain of the RPA70 subunit (RPA70N) interacts via a basic cleft with a wide range of DNA processing proteins, including several that regulate DNA damage response and repair. Small molecule inhibitors that disrupt these protein–protein interactions are therefore of interest as chemical probes of these critical DNA processing pathways and as inhibitors to counter the upregulation of DNA damage response and repair associated with treatment of cancer patients with radiation or DNA-damaging agents. Determination of three-dimensional structures of protein–ligand complexes is an important step for elaboration of small molecule inhibitors. However, although crystal structures of free RPA70N and an RPA70N–peptide fusion construct have been reported, RPA70N–inhibitor complexes have been recalcitrant to crystallization. Analysis of the $P6_1$ lattice of RPA70N crystals led us to hypothesize that the ligand-binding surface was occluded. Surface reengineering to alter key crystal lattice contacts led to the design of RPA70N E7R, E100R, and E7R/E100R mutants. These mutants crystallized in a $P2_12_12_1$ lattice that clearly had significant solvent channels open to the critical basic cleft. Analysis of X-ray crystal structures, target peptide binding affinities, and $^{15}N-^1H$ heteronuclear single-quantum coherence nuclear magnetic resonance spectra showed that the mutations do not result in perturbations of the RPA70N ligand-binding surface. The success of the design was demonstrated by determining the structure of RPA70N E7R soaked with a ligand discovered in a previously reported molecular fragment screen. A fluorescence anisotropy competition binding assay revealed this compound can inhibit the interaction of RPA70N with the peptide binding motif from the DNA damage response protein ATRIP. The implications of the results are discussed in the context of ongoing efforts to design RPA70N inhibitors.
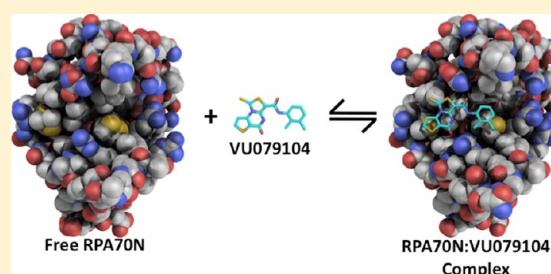
R eplication protein A (RPA) is the ubiquitous eukaryotic single-stranded (ss) DNA-binding protein that is essential for DNA replication, damage response, repair, and many other DNA transactions.[1,2] RPA functions to protect ssDNA from nucleolytic cleavage as well as prevent reannealing and formation of aberrant DNA structures.[3−6] RPA is a heterotrimer of RPA70, RPA32, and RPA14 subunits containing seven folded globular domains and one disordered domain (Figure 1). This modular structure allows it to interact simultaneously with the ssDNA substrate and partner proteins and thereby serve as a scaffold in a range of DNA processing machines. RPA interacts with other DNA processing proteins via the N, A, and B domains from the RPA70 subunit and the C domain from the RPA32 subunit.[7] RPA70N has previously been shown to be critical to the interaction of RPA with proteins involved in DNA damage response, including p53, ATRIP, RAD9, and MRE11.[8−11] RPA70N binds each of these proteins in a common basic cleft.[10]

The DNA damage response (DDR) is required to ensure proper maintenance and propagation of the genome.[12,13] Activation of the Ataxia Telangiectasia and Rad3-related protein
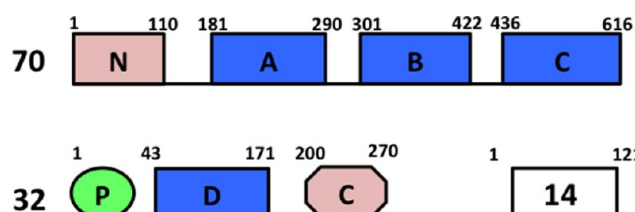

Figure 1. Subunit and domain structure of RPA. OB fold domains are depicted as rectangles; the winged helix–turn–helix domain is depicted as an octagon, and the unstructured phosphorylation domain is depicted as an oval. The ssDNA binding domains are RPA70A, -70B, -70C, and -32D (blue). Domains RPA70N and RPA32C are the primary protein recruitment modules (pink). The RPA trimer is formed by interactions among RPA70C, RPA32D, and RPA14.

(ATR) kinase plays a strategic role in DDR, for example, phosphorylating checkpoint protein Chk1 to halt cells in the S phase while DNA repair occurs.[10,14−17] ATR interacting protein (ATRIP) is an obligate cofactor required for stabilizing ATR, which also serves to recruit ATRIP to sites of DNA damage via interactions with RPA.[9,15] An RPA interaction motif near the N-terminus of ATRIP (residues 54−68) has been shown to interact with the basic cleft of RPA70N using nuclear magnetic resonance (NMR) spectroscopy.[10] This site therefore represents a potential target for the development of small molecules that inhibit RPA70N interactions.

A limited set of small molecule RPA70N ligands have already been reported on the basis of high-throughput screens.[18−23] However, the interaction of these compounds with RPA is quite weak (K_d in the micromolar range), and the molecular basis for binding has not been defined. Structural information about RPA70N−ligand complexes would greatly enhance the ability to develop inhibitors with substantially higher affinity, which is required for an effective inhibitor in cells. Although RPA70N readily crystallizes and the structure of it and that of a fusion of RPA70N to a peptide fragment of p53 have been determined,[24] complexes of RPA70N with fragments of other protein targets and of small molecule ligands have yet to be crystallized.

Here we describe the design, production, and characterization of RPA70N mutants that crystallize in an alternate lattice. To demonstrate the effectiveness of our approach, one of the mutant proteins is crystallized in complex with a previously identified ligand that competes with the RPA70N interaction motif from ATRIP.[25] This first structure of the complex of RPA70N with a small molecule lead inhibitor sets the stage for systematic structure-based design to generate more potent compounds.

■ MATERIALS AND METHODS

Site-Directed Mutagenesis, Growth, and Purification of RPA70N Mutants. The production of wild-type (WT) RPA70(1−120) from a pET15b vector (Novagen) was reported previously.[15] Primers (Sigma) for preparing the E7R, E100R, and E7R/E100R mutations were used with a Quick-Change Site-Directed Mutagenesis Kit (Stratagene). The mutated plasmids were transformed into BL21-DE3 cells (New England Biolaboratories) for expression. Growth and purification of unlabeled and ^{15}N-enriched RPA70N were performed as for the WT protein.[10]

Synthesis of VU079104. To a vial containing a solution of methyl 3-isothiocyanatothiophene-2-carboxylate (0.5 g, 2.5 mmol, 1 equiv) in DMF (1 mL) was added a solution of 2-cyano-N-(2,3-dimethylphenyl)acetamide (0.47 g, 2.5 mmol, 1 equiv) in DMF (1 mL). To this were added sulfur (0.08 g, 2.5 mmol, 1 equiv) and triethylamine (0.3 mL), and the reaction mixture was heated at 50 °C for 1 h. Once the reaction had reached completion as determined by liquid chromatography and mass spectrometry, the mixture was allowed to cool to room temperature and poured into a 3% AcOH solution. The solid formed was filtered and washed with methanol to give 0.45 g (46% yield) of pure N-(2,3-dimethylphenyl)-5-oxo-1-thioxo-4,5-dihydro-1H-thiazolo[3,4-a]thieno[2,3-e]pyrimidine-3-carboxamide (Figure S1 of the Supporting Information) as a yellow solid: ^{1}H NMR (400 MHz, DMSO-d_6) δ 10.11 (br s, 1H), 9.41 (d, J = 5.2 Hz, 1H), 8.30 (d, J = 5.2 Hz, 1H), 7.13 (m, 3H), 2.28 (s, 3H), 2.10 (s, 3H); ^{13}C NMR (125 MHz, DMSO-d_6) δ 181.0, 160.5, 155.2, 144.7, 141.1, 138.2, 135.5,

133.5, 129.0, 126.4, 125.6, 121.6, 120.7, 21.0, 15.1; high-resolution mass spectroscopy [M + H$^+$] calcd for $C_{17}H_{13}N_3O_2S_3$ 388.0248, found 388.0247.

Crystallization, Data Collection, and Refinement. Crystals of RPA70N E7R, E100R, and E7R/E100R were grown by sitting drop vapor diffusion at 21 °C from a drop composed of equal volumes of protein (7 mg/mL) and reservoir solution. Precipitant solution conditions were as follows: E7R, 100 mM MES (pH 6.5), 200 mM calcium acetate, and 20% PEG 8000; E100R, 100 mM BIS-TRIS (pH 5.5) and 2 M ammonium sulfate; E7R/E100R, 100 mM citrate (pH 5.0), 200 mM NaCl, and 30% PEG 8000. Prior to data collection, crystals were soaked in mother liquor containing 20% 2-methyl-2,4-pentanediol (MPD) and flash-frozen in liquid nitrogen. X-ray diffraction data were initially collected on an in-house rotating anode source and later at sector 21 [Life Sciences Collaborative Access Team (LSCAT)] at the Advanced Photon Source (Argonne National Laboratory, Argonne, IL). All data were processed with HKL2000.[26] The proteins crystallized in space group $P2_12_12_1$ and contained one molecule in the asymmetric unit. Initial phases were obtained by molecular replacement with PHASER[26,27] using the WT RPA70N structure [Protein Data Bank (PDB) entry 2B29] as a search model. Iterative cycles of model building and refinement were performed using COOT and Phenix.[28,29] The structures of RPA70N E7R, E100R, and E7R/E100R have been deposited in the Protein Data Bank as entries 4IPC, 4IPD, and 4IPG, respectively.

Crystallization and Refinement of the VU079104−RPA70N E7R Complex. Crystals of RPA70N E7R were grown using solution conditions described above. After the crystals had grown for 3 days, 1 μL of 50% PEG 8000 was added to the crystal drop and allowed to incubate for 15 min, after which 0.5 μL of 40 mM VU079104 in 100% dimethyl sulfoxide (DMSO) was added for 18 h. Prior to data collection at LSCAT, MPD was added to a final concentration of 15% and the crystal was flash-frozen in liquid nitrogen. Procedures identical to those described above for collection of the E7R structure were used with the exception that the structure of the mutant was used to obtain initial phase information. Following modeling of waters, VU079104 was placed into electron density at the basic cleft and refined. The structure of this complex has been deposited in the Protein Data Bank as entry 4IPH.

Calculation of Surface Electrostatic Charges. Electrostatic surfaces were calculated using the APBS[30] plug-in of Pymol (Scrödinger) using a grid centered upon the center of mass of WT, E7R, E100R, or E7R/E100R. Grid lengths of 74.54 Å × 81.5 Å × 56 Å and 63.8 Å × 68 Å × 53 Å were used as coarse and fine grid calculation inputs, respectively. Default APBS settings were used for solvent radius, dielectric, temperature, ionic strength, and radius.

NMR Spectroscopy. NMR spectra were acquired using a Bruker AVANCE III 600 MHz spectrometer equipped with a CPQCI cryoprobe. ^{15}N-enriched WT and mutant RPA70N proteins were prepared in a solution containing 50 mM HEPES (pH 7.5) with 100 mM NaCl and 5 mM DTT, while an identical solution supplemented with 5% DMSO was used for titrations of VU079104 into WT RPA70N. Two-dimensional ^{15}N−^{1}H heteronuclear single-quantum coherence (HSQC) spectra were acquired with 128 and 1024 complex points in the ^{15}N and ^{1}H dimensions, respectively. Titration experiments were performed using an initial protein concentration of 150 μM with spectra collected at ATRIP$_{54−86}$ concentrations of 0,

50 100, 200, 385, 740, and 1070 μM or at VU079104 concentrations of 0, 2, 6, 14, 54, 132, 288, 517, and 1034 μM. Data were processed using NMRpipe[31] and analyzed with Sparky (University of California, San Francisco, CA). ^{1}H and ^{15}N backbone NMR assignments for RPA70N were reported previously.[10,15] Chemical shift perturbations were analyzed using a weighted average of the change in chemical shift ($\Delta\delta$) upon binding of ATRIP$_{54-68}$ or VU079104 based on the net perturbations in both the ^{1}H and ^{15}N dimensions calculated using eq 1:[32]

$$\Delta\delta\,(\text{ppm}) = \{(\Delta^1H)^2 + [\Delta^{15}N(0.2)]^2\}^{1/2} \qquad (1)$$

Fluorescence Polarization Anisotropy Displacement Assay. Fluorescein isothiocyanate (FITC)-labeled ATRIP peptide (FITC-Ahx-DFTADDLEELDTLAS-NH$_2$) amidated at its C-terminus was purchased from NeoBioSci (NEO Group) at >95% HPLC verified purity and reconstituted in DMSO to a final concentration of 1 mM. The peptide equilibrium dissociation constant for binding to WT and RPA70N mutants was determined using a fluorescence polarization anisotropy (FPA) experiment described previously.[25] Briefly, increasing concentrations of protein in assay buffer [50 mM HEPES (pH 7.5), 100 mM NaCl, and 5 mM DTT] were incubated with 50 nM FITC-ATRIP in a 96-well flat bottom black well plate (Thermo Fisher Scientific) at room temperature for 1 h. The fluorescence polarization measurements and inhibitor assays were performed using a Wallac 2100 EnVision plate reader (Perkin-Elmer). Data were acquired at an excitation wavelength of 480 nm and an emission wavelength of 535 nm. The emission anisotropy values were determined with Envision using formulas previously described.[25] For peptide or inhibitor binding assays, anisotropy values were plotted against RPA protein or VU079104 concentration and fit as described previously.[25] The dissociation constant (K_d) reported is an average of two independent experiments, each run in duplicate.

■ RESULTS

Our studies began with cocrystallization trials for RPA70N with small molecules from a high-throughput screen of potential inhibitors[25] using the known conditions for crystallizing the free protein. To drive the equilibrium from the free state toward the ligand-bound state, the compounds were added to a concentration >10-fold higher than their K_d values, i.e., 2 mM ligand in 250 μM solutions of RPA70N. Crystals were routinely observed within 2 days, but no ligand density was observed in any of the 50 different crystals that were evaluated. Similarly, we were unable to observe density for any ligand from 50 different soaks (5 h) into preformed WT RPA70N crystals.

We then systematically analyzed the effect of buffer conditions (pH, ionic strength, additives, and buffering agent) and temperature on the visual appearance of the RPA70N crystals with the goal of finding an alternate crystal morphology. Although all crystals remained in the previously reported hexagonal form,[24] we collected data sets for each to determine if any of these crystals exhibited different lattice packing contacts, but no differences were observed. We next turned to an analysis of the packing of RPA70N molecules in the hexagonal crystal lattice and observed that the key basic cleft is occluded, which presumably was inhibiting binding to this interaction surface (Figure 2A,B). We therefore hypothesized that charge reversal mutations of residues mediating intermolecular contacts would promote crystallization in a
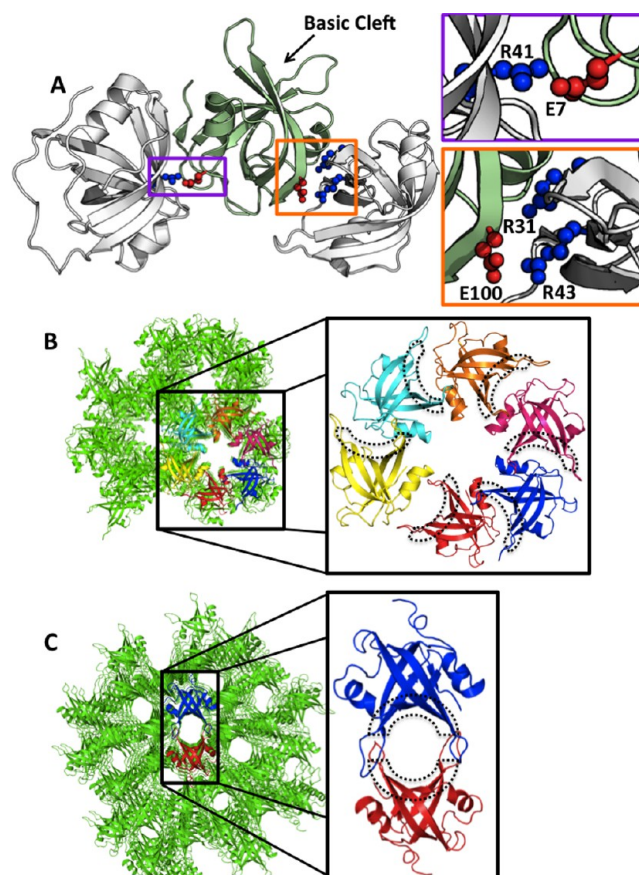

Figure 2. Packing of RPA70N in hexagonal and orthorhombic crystal lattices. (A) Lattice contacts in the hexagonal crystal lattice between residues E7 and E100 (red) and basic cleft residues R31, R41, and R43 (blue) from an adjacent RPA70N molecule. (B) Packing of the basic cleft of RPA70N against the backside of its symmetry mate in the hexagonal crystal lattice blocks access to the basic cleft (dashed line). (C) Packing in the orthorhombic lattice adopted by RPA70N charge reversal mutants produces solvent channels formed directly by the basic clefts (dashed line) of opposing RPA70N symmetry mates.

lattice better suited to obtaining crystals of the protein−ligand complexes.

E7R, E100R, and E7R/E100R Mutations Produce Crystals in a Lattice Amenable to Soaking. Inspection of the contacts between RPA70N molecules in the crystal revealed that basic cleft residues R31, R41, and R43 contacted E7 and E100 from adjacent molecules (Figure 2A). We therefore created and purified charge reversal mutants E7R and E100R and double mutant E7R/E100R. Standard crystallization trials produced crystals within 72 h, and inspection under a dissecting light microscope revealed crystal morphologies visibly different than those observed for WT RPA70N. After diffraction data had been indexed, all three mutants were found to have crystallized in an orthorhombic $P2_12_12_1$ space group. Comparison of the crystal lattices revealed that, unlike the hexagonal crystal lattice observed for WT RPA70N, the basic cleft was exposed to a solvent channel and accessible for binding target peptides and small molecules (Figure 2C). Notably, the $P2_12_12_1$ lattice is the same as that found for the RPA70N−p53 peptide fusion construct with RPA70N arrayed in a similar manner.[8]

X-ray crystal structures of E7R, E100R, and E7R/E100R were determined using the molecular replacement approach

Table 1. Model Statistics[a]

	E7R RPA70N	E100R RPA70N	E7R/E100R RPA70N	E7R RPA70N−compound
PDB entry	4IPC	4IPD	4IPG	4IPH
		Data Collection		
wavelength (Å)	0.97857	0.97857	0.97857	0.97857
space group	$P2_12_12_1$	$P2_12_12_1$	$P2_12_12_1$	$P2_12_12_1$
cell dimensions				
a, b, c (Å)	38.54, 53.72, 54.36	39.43, 50.15, 51.87	38.49, 53.79, 54.38	38.27, 54.27, 54.33
α, β, γ (deg)	90, 90, 90	90, 90, 90	90, 90, 90	90, 90, 90
resolution (Å)	50−1.22	50−1.51	50−1.58	50−1.94
R_{sym} (%)	5.7	9.9	6.5	10.6
I/dI	15.37 (2.55)	40.38 (17.41)	18.30 (2.54)	14.33 (2.91)
completeness (%)	99.72 (99.97)	99.24 (96.00)	99.92 (100.00)	98.31 (97.70)
redundancy	5.9 (5.9)	8.4 (8.0)	5.9 (5.9)	5.7 (5.7)
		Refinement		
resolution (Å)	31.44 (1.22)	36.05 (1.51)	24.27 (1.58)	31.28 (1.94)
no. of reflections	202226	139424	94894	49814
R_{work} (%)	14.74 (20.03)	13.76 (14.08)	16.34 (19.53)	19.63 (22.62)
R_{free} (%)	17.55 (25.35)	16.59 (18.63)	20.07 (23.86)	27.37 (31.26)
no. of atoms	2322	2288	2210	1113
protein	1049	1030	987	955
ligand	−	−	−	50
water	123	156	148	108
B factor (Å^2)				
average	20.2	10.7	19.8	24.7
protein	18.8	9	17.8	21.9
water	31.5	22.5	33.2	34.3
bonds (RMS deviation)				
bond lengths (Å)	0.009	0.007	0.018	0.011
bond angles (deg)	1.37	1.3	1.8	1.26
Ramachandran plot (%)				
most favored	96	97	98	98
allowed	3.3	3	2	2
disallowed	0.7	0	0	0

[a]Values in parentheses refer to those in the highest-resolution shell.

with WT RPA70N as the search model. The diffraction data were refined to 1.22, 1.51, and 1.58 Å resolution, respectively, i.e., at effectively the same or higher resolution than the resolution of 1.60 Å obtained for WT RPA70N. Structural statistics are listed in Table 1. All three mutants adopt the OB fold structure characterized by a five-stranded β-sheet coiled to form a closed β-barrel capped by α-helices (Figure 3). The data were refined at high resolution, which included modeling of alternative side chain conformations at multiple sites in all three structures.

Evaluation of E7R, E100R, and E7R/E100R Mutants as Models for WT RPA70N. The structures of the mutants are all very similar to each other and to that of WT RPA70N. The pairwise Cα root-mean-square deviations (rmsds) between the mutants are 0.27 Å (E7R vs E100R), 0.20 Å (E7R vs E7R/E100R), and 0.22 Å (E100R vs E7R/E100R). Superposition of the mutants with WT RPA70N for E7R, E100R, and E7R/E100R produced all Cα atom rmsd's of 0.45, 0.43, and 0.42 Å, respectively (Figure 3). Slight shifts of flexible loop residues located between β-sheets 1 and 2 and β-sheets 4 and 5 were also noted upon comparison of the structures to that of WT RPA70N. These shifts are attributed to the new crystal lattice contacts made in the orthorhombic crystal lattice as they involve a set of residue contacts different from those used by the loops in the WT RPA70N hexagonal crystal lattice. A number of new crystal contacts formed by the charge reversal
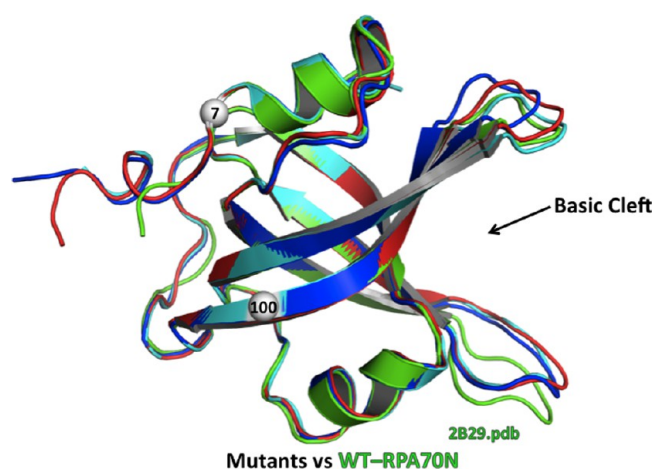

Figure 3. Comparison of the structures of WT RPA70N and the E7R, E100R, and E7R/E100R mutants. Best-fit superposition (Cα atoms) of the structures of E7R (red), E100R (blue), and E7R/E100R (cyan) on the structure of WT RPA70N (green).

mutations were also noted. In the case of E7R, R7 contacts (≤3.5 Å) T34, N85, and K88 of symmetry-related molecules. In E100R, R100 contacts Q15, S73, N74, G109, and E120 of symmetry-related molecules. Similarly, in the E7R/E100R mutant, R7 contacts T34, N85, and K88, and R100 contacts

S73, N74, G109, and E120 of symmetry-related molecules. Closer inspection revealed that even the most statistically significant differences are relatively modest; these occur primarily for solvent-exposed side chains that change rotamers, including R41, R43, and R91 (Figure S2 of the Supporting Information).

The structures of the RPA70N mutants were further assessed by calculating electrostatic surface potentials (Figure 4).
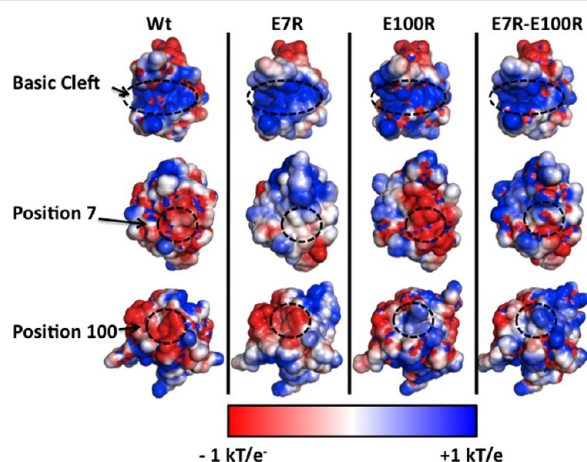

Figure 4. Electrostatic surface potentials of WT RPA70N and the E7R, E100R, and E7R/E100R mutants. Surface potentials were calculated using APBS software for WT, E7R, E100R, and E7R/E100R (from left to right, respectively). Dashed circles are drawn to highlight the basic cleft, residue 7, and residue 100.

Importantly, the basic clefts of the mutants are indistinguishable from WT RPA70N. Thus, as anticipated, charge reversal of E7 and E100 resulted in substantial changes in the electrostatic potential in the vicinity of the mutation sites. However, because these are at the opposite side of the molecule, these mutations did not significantly alter the critical ligand-binding surface of RPA70N.

To further validate the three mutants as suitable models for WT RPA70N, their interactions with the RPA interaction motif from the N-terminal region of ATR were investigated. Following our previously reported study,[15] ^{15}N−^{1}H HSQC NMR spectroscopy was used to determine the residues in the mutant proteins that were affected upon binding of ATRIP$_{54-68}$ (Figure 5A and Figure S3 of the Supporting Information). The NMR chemical shift perturbations observed were nearly identical in all three mutant proteins and corresponded well to those observed in a corresponding titration of WT RPA70N. Indeed, the magnitude of chemical shift perturbations calculated in terms of global chemical shift correlation is similar (Figure 5B). The slope of these plots provides correlations to WT of 1.01, 1.04, and 1.01 for E7R, E100R, and E7R/E100R, respectively, indicating a very high degree of structural similarity among the complexes with ATRIP$_{54-68}$.

Our previously developed fluorescence polarization anisotropy (FPA) assay was then used to measure the binding affinity of ATRIP$_{54-68}$ for WT, E7R, E100R, and E7R/E100R (Figure S4 of the Supporting Information).[25] Binding curves were generated by fitting anisotropy values to a single-site binding model and yielded binding affinities that were very similar to each other (Table 2). These data confirmed that the charge reversal mutations designed to alter the crystal packing do not alter the target binding properties of RPA70N.
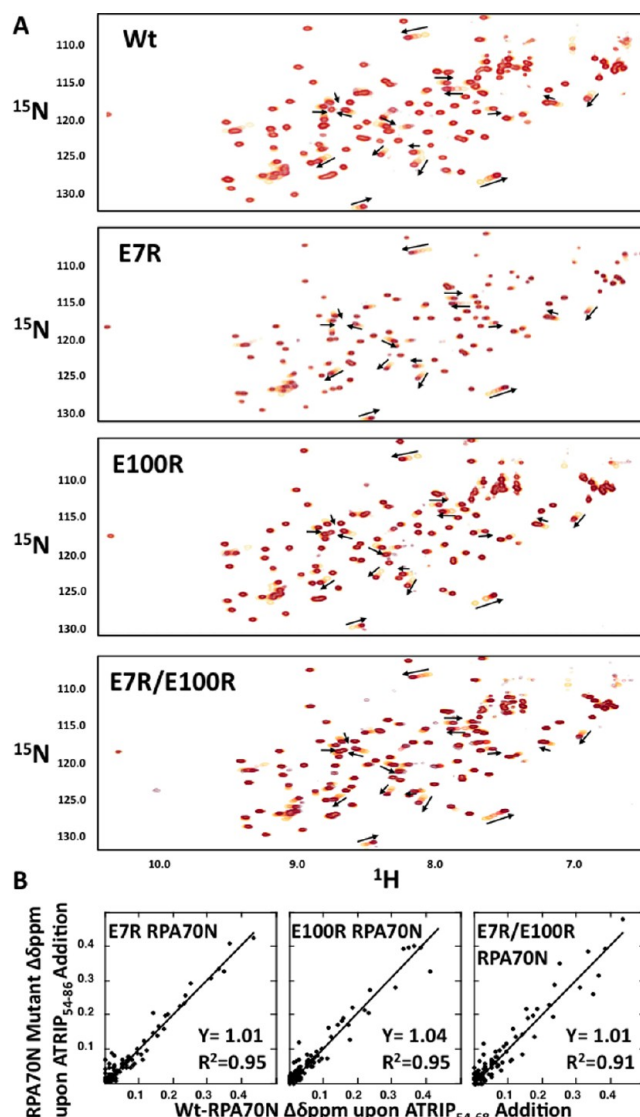

Figure 5. Comparison of NMR chemical shift perturbations induced by binding of ATRIP$_{54-68}$ in WT RPA70N and the E7R, E100R, and E7R/E100R mutants. (A) NMR titration with ATRIP$_{54-68}$. Overlay of ^{15}N−^{1}H HSQC spectra of WT RPA70N and the E7R, E100R, and E7R/E100R mutants as ATRIP$_{54-68}$ is titrated into the sample. ^{15}N−^{1}H cross-peaks are colored from yellow to dark red as ATRIP$_{54-68}$ is added. Arrows indicate the starting and ending points for select residues exhibiting significant chemical shift perturbations. (B) Correlation plots comparing the chemical shift perturbations in complexes of ATRIP$_{54-68}$ with mutant (y-axis) and WT (x-axis) RPA70N.

Table 2. Affinity of RPA70N for ATRIP$_{54-68}$

RPA70N construct	K_d (μM)
WT	5.61 ± 0.84
E7R	5.01 ± 0.30
E100R	7.67 ± 0.32
E7R/E100R	3.64 ± 0.54

Overall, these analyses show that the structures of the mutants are very similar to that of the WT protein and in particular that the key ligand-binding site is not perturbed. Hence, reengineering of the surface charge to disrupt the hexagonal crystal lattice was successful and generated the
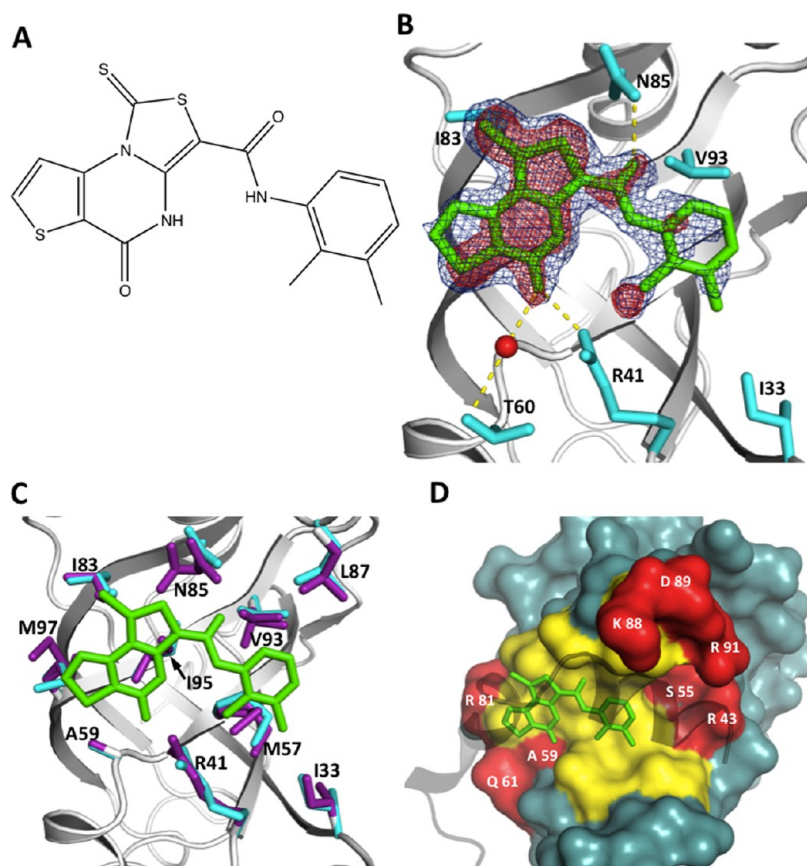
Figure 6. Structure of RPA70N E7R in complex with VU079104. (A) Chemical structure of VU079104. (B) Structure of RPA70N E7R colored to highlight side chains (cyan) within 3.5 Å of VU079104 (green), a crystallographic water (red sphere), and hydrogen bonding interactions with VU079104 (yellow dashes). VU079104 $2F_o − F_c$ and $F_o − F_c$ electron density maps contoured at 1σ and 3σ are colored blue and red, respectively. (C) Changes in E7R side chains induced by binding of the ligand. The overlay shows the positioning of side chains within 3.5 Å of VU079104 (green) for E7R (purple sticks) and the E7R−VU079104 complex (cyan). (D) Superposition of VU079104 (sticks) from the structure of the complex onto the surface of the structure of the RPA70N−p53 complex (PDB entry 2B3G). Solvent-exposed surface residues within 4 Å of VU079104 and the p53 peptide (black) are colored yellow and red, respectively.

desired model for cocrystallization of WT RPA70N with target peptides and small molecule ligands.

Structure of a VU079104−E7R Complex. To demonstrate that structures of ligand complexes could be obtained, we cocrystallized E7R with VU079104 from our previously reported molecular fragment screen[25] and determined the X-ray crystal structure (Figure 6A). Because the affinity of small molecules for RPA70N is typically in the micromolar range, our crystallization strategy involved soaking preformed crystals of E7R in a solution containing 10 mM ligand to promote saturation of all protein molecules. The E7R mutant was selected for this experiment because it produced the largest crystals among the three mutants. The crystals were soaked for 18 h, after which they were harvested and flash-frozen in liquid nitrogen and screened for diffraction. Full data sets were collected for all such crystals, and after initial refinement of the best diffracting crystal, electron density was clearly evident in the basic cleft (Figure 6B). The density was readily fit with the VU079104 ligand, and after optimization, the structure was refined to a final resolution of 1.94 Å (Table 1).

The backbone of E7R did not change significantly upon ligand binding, but multiple side chains did reorient to accommodate VU079104 within the basic cleft. Two molecules of VU079104 were identified per molecule of E7R within the asymmetric unit. One ligand molecule makes numerous

intermolecular contacts within the basic cleft (Figure 6B), including notable hydrophobic contacts with I33, V93, and I95, as well as two direct hydrogen bonds to R41 and N85. The positions of the latter two residues are shifted upon binding of the ligand with the side chain of R41 moving by 0.9 Å and that of N85 shifting from multiple side chain conformations to occupying a single rotamer (Figure 6C). In contrast, the second VU079104 molecule had no significant contact with the protein.

The second molecule became apparent only after placement of the first VU079104 molecule into the $F_o − F_c$ electron density map. The additional $F_o − F_c$ electron density corresponded well to another VU079104 molecule. This second molecule makes hydrophobic π-stacking interactions with the first molecule of VU79104 in a slightly offset orientation, which presumably maximizes the favorable aromatic stacking interactions (Figure S5 of the Supporting Information). The second VU079104 molecule is likely an artifact of crystallization and is possible because the solvent channel within the orthorhombic crystal lattice is quite large. The only interaction with the protein is one weak contact to the side chain η-nitrogen of R41 at 3.4 Å.

VU079104 Interacts with the Basic Cleft of RPA70N in Solution. Although the structure of the E7R−VU079104 complex shows the ligand bound in the basic cleft, it is
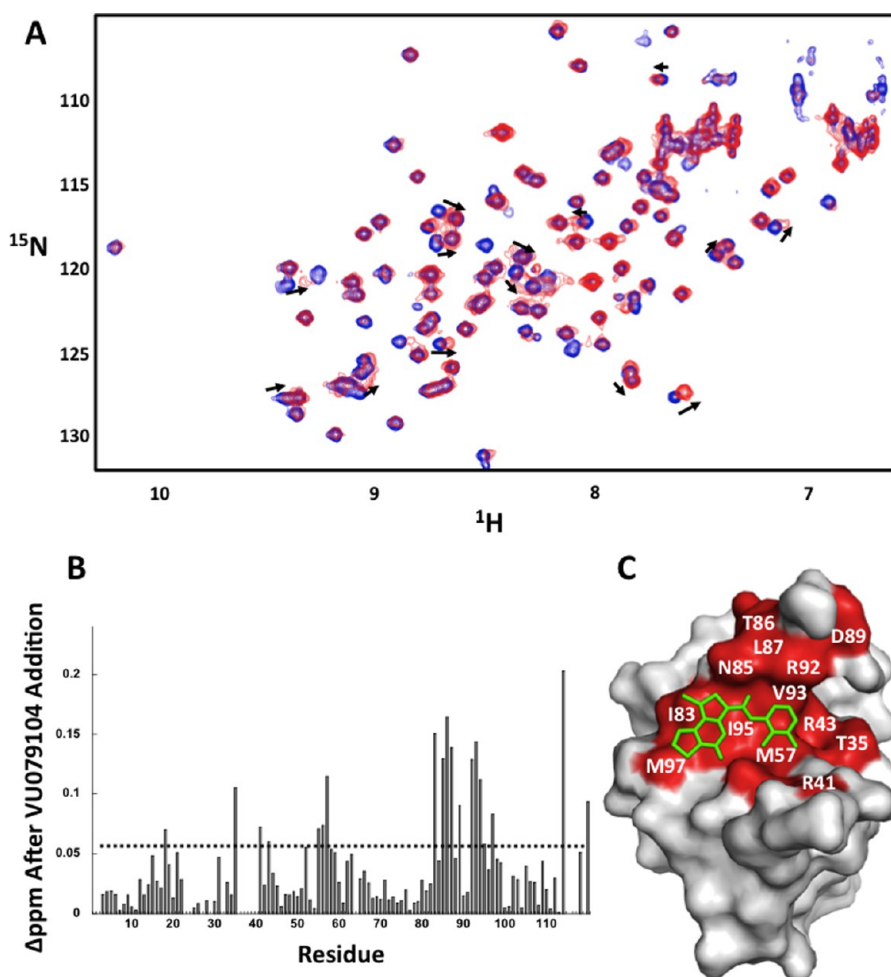
Figure 7. $^{15}N-^{1}H$ chemical shift changes in WT RPA70N induced by binding of VU079104. (A) Overlaid $^{15}N-^{1}H$ spectra of WT RPA70N (blue) and VU079104-saturated WT RPA70N (red), where arrows indicate the direction of movement of select $^{15}N-^{1}H$ cross-peaks. (B) Quantified chemical shift perturbations induced upon binding of VU079104 to WT RPA70N. (C) Locations of significantly perturbed WT RPA70N residues (red) upon addition of VU079104 mapped upon the structure of RPA70N E7R in complex with VU079014 (green sticks).

important to confirm that this is the actual binding site in solution. Consequently, a $^{15}N-^{1}H$ HSQC NMR titration was used to map residues whose chemical environment was perturbed upon binding of VU079104 (Figure 7A). The observation of RPA70N chemical shift perturbations within the fast exchange limit over the course of the titration is consistent with binding of the ligand in the micromolar regime. Mapping of the chemical shift perturbations onto the crystal structure of E7R in the VU079104 complex (Figure 7B,C) shows the expected binding in the basic cleft. These data indicate that the binding site for VU079104 is the same in the crystal and solution, demonstrating that soaking into preformed crystals can be readily accommodated by the basic cleft of RPA70N.

VU079104 Inhibits Binding of the ATRIP Interaction Motif. To investigate if VU079104 is capable of inhibiting protein−protein interactions, we performed our previously described fluorescence anisotropy assay.[25] This competition-based assay uses a FITC-labeled ATRIP$_{54-68}$ peptide, which was shown to undergo a large change in fluorescence anisotropy upon binding to RPA70N and a return to the starting state when another molecule is able to displace the peptide from the protein. Figure 8 shows the displacement curve obtained when VU079104 is titrated into the solution of the RPA70N−peptide complex. Fitting of these data to a
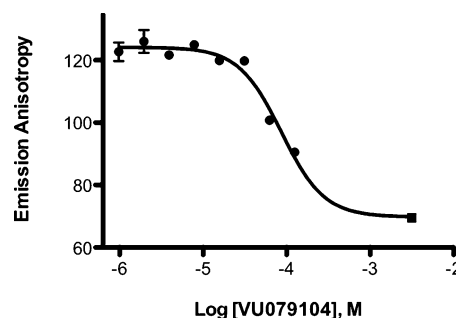

Figure 8. Fluorescence polarization anisotropy assay of the displacement of ATRIP$_{54-68}$ from RPA70N by VU079104. Concentration−response curve used for determination of the K_d for binding of VU079104 to WT RPA70N. The error bars represent standard deviations of two independent experiments, each performed in duplicate. The data point represented by the square corresponds to the anisotropy value recorded for ATRIP$_{54-68}$ in the absence of RPA70N.

standard single-site binding equation provides a K_d of 41.4 ± 3.2 μM. These data show VU079104 is capable of displacing the peptide from the basic cleft of RPA70N. This result, combined with the crystal structure of the complex and our NMR analyses, indicates that VU079104 represents a viable

initial lead compound for the development of an RPA70N inhibitor.

Structure-Based Leads for Elaboration of VU079104. Previous studies by our laboratory have established a common set of residues within the RPA70N basic cleft that are used for binding ATRIP, Rad9, and MRE11.[10] Our structure of the RPA70N−VU079104 complex shows that this ligand binds directly in the basic cleft and orients itself by hydrogen bonding with R41 and N85. Notably, many of the same hydrophobic contacts utilized to bind VU079104 are also made in the complex with the p53 peptide.[24] This suggests VU079104 is a viable scaffold upon which chemical modifications can be introduced to produce a more potent RPA70N inhibitor.

Comparison of RPA70N binding interface residues located within 4 Å of VU079104 to those utilized in the binding of the p53 peptide (Figure 6D) reveals solvent-exposed surfaces surrounding VU079104 that can be utilized to produce analogues of increased affinity. Using the contact surface of p53 in the basic cleft of RPA70N as a guide, possible routes for elaboration of the molecule can be envisioned. It is well-known that RPA70N interaction motifs are acidic.[10] In this vein, VU079104 can be extended with carboxylate functional groups directed toward basic residues R41 and/or R81. Incorporation of this favorable charge−charge interaction into the three-membered ring system will likely offer a reasonable increase in affinity. A more significant increase in affinity may be realized through occupation of the hydrophobic pocket centered on S55 (Figure 6D). Addition of a phenyl group to the 2,3-dimethylphenyl ring of VU079104 via a linker of appropriate length would mimic the structure of the RPA70N−p53$_{44−58}$ fusion protein, as F54 makes hydrophobic contacts in this pocket (Figure 9) and buries 74.9 Å^2 of the solvent-exposed
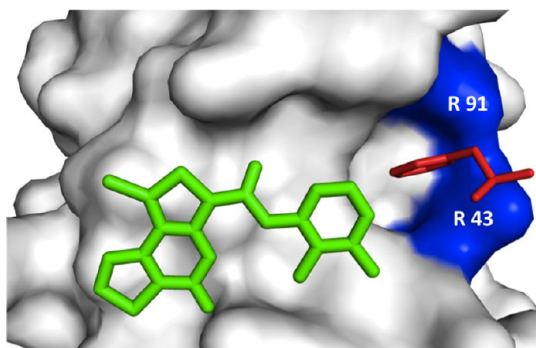

Figure 9. Comparative structural analysis suggests targeting of the S55 pocket to increase the affinity of the VU079104 framework for RPA70N. Superposition of VU079104 onto the surface of the structure of the RPA70N−p53 peptide fusion (PDB entry 2B3G) showing the proximity of VU079104 to the hydrophobic pocket into which the F54 ring of p53 is inserted (red) and a basic patch on RPA70N created by residues R43 and R91 (blue).

hydrophobic surface. Additional potential salt bridge interactions or hydrogen bonds with nearby RPA70N residues R43 and R91 represent attractive additional stabilizing interactions because these residues have been shown previously to play important roles in target binding[10] (Figure 9).

■ DISCUSSION

Small molecule discovery is greatly aided by the availability of high-resolution structures of protein−ligand complexes.[33] The pursuit of such an approach is highly relevant for efforts to identify effective inhibitors of RPA70N, as direct high-throughput screens have yet to turn up compounds with affinities in the desired nanomolar range. It is well-known that crystal packing can inhibit the binding of ligands when the critical protein surfaces are rendered inaccessible by lattice contacts, as is seen here for crystals of WT RPA70N. Alternate crystal morphologies can be produced sometimes by changing the solution used for crystallization. However, screening of more than 500 sparse matrix crystallization conditions for RPA70N did not produce any alternate crystal forms. An alternate crystal morphology was produced in the previously reported structure of an RPA70N−p53 fusion construct.[24] However, covalent linkage of VU079104 and other fragment lead molecules is not routinely feasible and would likely bias the resulting structure.

Two common approaches for disrupting the crystal packing contacts that favor an unwanted crystal form are reengineering residues at the protein surface and fusing the protein of interest to a known highly crystallizable protein (reviewed in refs 34−37). Fusion of RPA70N to maltose binding protein or lysozyme was not applied here because tethering may have blocked the ligand-binding surface. Aside from the protein fusion strategy, the other strategies are based on targeting solvent-exposed surface residues, which are the mediators of crystal lattice contact points. Mutation of Arg and Lys residues to reduce surface entropy is a common approach.[39] This was not chosen for our system because the most obvious crystal contacts in the lattice of the WT protein are from Arg and Lys residues in the critical basic cleft of RPA70N where our inhibitors need to bind. Recently, systematic mutagenesis of surface residues and/or deletion of loops and disordered regions has been used to produced a significantly higher-resolution structure for a complex of the HIV reverse transcriptase and a small molecule inhibitor TMC278.[38] Although this highly systematic approach was successful, in reference to RPA70N, care would be needed to avoid perturbing the critical basic cleft. Moreover, this study required the generation, expression, and crystallization of >60 different protein constructs.

The approaches noted above do not require knowledge of the three-dimensional structure of the protein of interest and have proven to be relatively robust. However, when the structure is available, it is possible to examine the specific crystal lattice contacts and design modifications to the surface residues involved in a highly targeted and efficient manner. Inspection of the structure of WT RPA70N revealed that in its $P6_1$ lattice, the key residues in the basic cleft mediate crystal lattice contacts, interacting with acidic residues on the opposite face of another RPA70N molecule. We therefore designed charge reversal mutations of acidic residues E7 and E100, which are distant from the basic cleft, and found that these are sufficient to achieve the goal of producing the change in crystal lattice packing with minimal alteration of RPA70N. A similar approach employing charge neutralization of surface glutamate residues has been reported in a recent study of the Kelch domain of human Keap1.[40] We note that in contrast to a number of other surface reengineering studies in which more than one surface mutation or tethering to another protein was required to induce alternate crystal lattice packing,[38,41−43] a single point mutation at E7 or E100 was sufficient to generate the new crystal packing lattice for RPA70N.

The effects of a mutation on the physical properties of a protein should always be investigated to ensure that the mutant

represents an accurate model for the WT protein. WT RPA70N carries a net charge of zero with a pI of 6.93, whereas the charge reversal mutants have relative net charges of +1 (E7R and E100R) and +2 (E7R/E100R) with pI values of 8.73 and 9.44, respectively. No significant perturbations were observed in the high-resolution crystal structures of any of the mutants. Increasing the net positive charge of RPA70N could conceivably affect long-range electrostatic interactions, particularly as all known RPA70N ligands have an electrostatic component to binding. However, we note that no significant differences with respect to the WT protein were observed in the binding affinities of the mutants for the highly acidic ATRIP peptide (net charge of −6). This observation is consistent with the electrostatic field potentials calculated at the ligand-binding surface, which predict no differences in electrostatic field in the basic cleft between the mutants and WT protein (Figure 4).

The increase in resolution obtained for E7R correlates with a more ordered and stable crystalline lattice. This added stability of the lattice provides an extra benefit for the soaking of small organic molecules such as VU079104, which are commonly dissolved in DMSO. This extra stability of the lattice proved to be valuable in this case as 25% DMSO is required for generating a saturated solution of VU079104. Hence, initial attempts to soak the ligand into WT RPA70N crystals led to dissolution of the crystal. In contrast, the more stable crystal lattice attained for E7R is more tolerant of DMSO and affords the opportunity to determine the structures of complexes with other ligands having limited aqueous solubility.

CONCLUSIONS

The studies described here establish for the first time a structural basis for inhibition of the basic cleft of RPA70N. We showed that VU079104 is capable of displacing a peptide derived from DNA damage response protein ATRIP. In addition, the results presented here validate the use of RPA70N charge reversal mutants E7R, E100R, and E7R/E100R as suitable artifact-free crystallization platforms that can be used in future structure-based inhibitor design efforts.

DNA damage response and repair are upregulated in response to radiation and chemotherapy treatments, which elicit their effect by damaging DNA. Because accumulation of RPA-coated ssDNA is a signal for the initiation of the DNA damage response, RPA70N inhibitors that block interactions with key partner proteins could disrupt the mobilization of the DNA damage response proteins and restart of stalled replication forks. RPA70N inhibitors that suppress the DNA damage response and subsequent repair therefore have the potential to sensitize cancer cells to the DNA-damaging agents that are currently being used to treat cancer patients. Thus, the RPA70N mutants presented here are of considerable value to ongoing structure-based discovery efforts aimed at generating RPA70N inhibitors with therapeutic potential for the treatment of cancer.

ASSOCIATED CONTENT

Ⓢ Supporting Information

Synthesis of VU079104, alternative conformations of select E7R, E100R, and E7R/E100R RPA70N residues, NMR analysis, fluorescence polarization anisotropy assays, and electron density of the second molecule of VU079104. This material is available free of charge via the Internet at http://pubs.acs.org.

Accession Codes

Atomic coordinates and structure factors for the crystal structures of RPA70N E7R, E100R, E7R/E100R, and E7R in complex with VU079104 have been deposited as Protein Data Bank entries 4IPC, 4IPD, 4IPG, and 4IPH, respectively.

AUTHOR INFORMATION

Corresponding Author

*E-mail: walter.chazin@vanderbilt.edu. Phone: (615) 936-2210.

Present Address

[⊥]A.O.F.: Global Discovery Chemistry, Novartis Institutes for BioMedical Research (NIBR), Emeryville, CA 94608-2916.

REFERENCES

(1) Wold, M. S., and Kelly, T. (1988) Purification and characterization of replication protein A, a cellular protein required for in vitro replication of simian virus 40 DNA. *Proc. Natl. Acad. Sci. U.S.A. 85*, 2523−2527.

(2) Wold, M. S. (1997) Replication protein A: A heterotrimeric, single-stranded DNA-binding protein required for eukaryotic DNA metabolism. *Annu. Rev. Biochem. 66*, 61−92.

(3) Bochkarev, A., Pfuetzner, R. A., Edwards, A. M., and Frappier, L. (1997) Structure of the single-stranded-DNA-binding domain of replication protein A bound to DNA. *Nature 385*, 176−181.

(4) Lao, Y., Gomes, X. V., Ren, Y., Taylor, J. S., and Wold, M. S. (2000) Replication protein A interactions with DNA. III. Molecular basis of recognition of damaged DNA. *Biochemistry 39*, 850−859.

(5) Treuner, K., Ramsperger, U., and Knippers, R. (1996) Replication protein A induces the unwinding of long double-stranded DNA regions. *J. Mol. Biol. 259*, 104−112.

(6) Zou, L., Liu, D., and Elledge, S. J. (2003) Replication protein A-mediated recruitment and activation of Rad17 complexes. *Proc. Natl. Acad. Sci. U.S.A. 100*, 13827−13832.

(7) Fanning, E., Klimovich, V., and Nager, A. R. (2006) A dynamic model for replication protein A (RPA) function in DNA processing pathways. *Nucleic Acids Res. 34*, 4126−4137.

(8) Dutta, A., Ruppert, J. M., Aster, J. C., and Winchester, E. (1993) Inhibition of DNA replication factor RPA by p53. *Nature 365*, 79−82.

(9) Cortez, D., Guntuku, S., Qin, J., and Elledge, S. J. (2001) ATR and ATRIP: Partners in checkpoint signaling. *Science 294*, 1713−1716.

(10) Xu, X., Vaithiyalingam, S., Glick, G. G., Mordes, D. A., Chazin, W. J., and Cortez, D. (2008) The basic cleft of RPA70N binds multiple checkpoint proteins, including RAD9, to regulate ATR signaling. *Mol. Cell. Biol. 28*, 7345−7353.

(11) Lee, S. E., Moore, J. K., Holmes, A., Umezu, K., Kolodner, R. D., and Haber, J. E. (1998) *Saccharomyces* Ku70, mre11/rad50 and RPA proteins regulate adaptation to G2/M arrest after DNA damage. *Cell 94*, 399−409.

(12) Nam, E. A., and Cortez, D. (2011) ATR signalling: More than meeting at the fork. *Biochem. J. 436*, 527−536.

(13) Bensimon, A., Aebersold, R., and Shiloh, Y. (2011) Beyond ATM: The protein kinase landscape of the DNA damage response. *FEBS Lett. 585*, 1625−1639.

(14) Namiki, Y., and Zou, L. (2006) ATRIP associates with replication protein A-coated ssDNA through multiple interactions. *Proc. Natl. Acad. Sci. U.S.A. 103*, 580−585.

(15) Ball, H. L., Ehrhardt, M. R., Mordes, D. A., Glick, G. G., Chazin, W. J., and Cortez, D. (2007) Function of a conserved checkpoint recruitment domain in ATRIP proteins. *Mol. Cell. Biol. 27*, 3367−3377.

(16) Ball, H. L., Myers, J. S., and Cortez, D. (2005) ATRIP binding to replication protein A-single-stranded DNA promotes ATR-ATRIP localization but is dispensable for Chk1 phosphorylation. *Mol. Biol. Cell 16*, 2372−2381.

(17) Olson, E., Nievera, C. J., Klimovich, V., Fanning, E., and Wu, X. (2006) RPA2 is a direct downstream target for ATR to regulate the S-phase checkpoint. *J. Biol. Chem. 281*, 39517−39533.

(18) Anciano Granadillo, V. J., Earley, J. N., Shuck, S. C., Georgiadis, M. M., Fitch, R. W., and Turchi, J. J. (2010) Targeting the OB-Folds of Replication Protein A with Small Molecules. *J. Nucleic Acids 2010*, 304035.

(19) Shuck, S. C., and Turchi, J. J. (2010) Targeted inhibition of replication protein A reveals cytotoxic activity, synergy with chemotherapeutic DNA-damaging agents, and insight into cellular function. *Cancer Res. 70*, 3189−3198.

(20) Andrews, B. J., and Turchi, J. J. (2004) Development of a high-throughput screen for inhibitors of replication protein A and its role in nucleotide excision repair. *Mol. Cancer Ther. 3*, 385−391.

(21) Glanzer, J. G., Liu, S., and Oakley, G. G. (2011) Small molecule inhibitor of the RPA70 N-terminal protein interaction domain discovered using in silico and in vitro methods. *Bioorg. Med. Chem. 19*, 2589−2595.

(22) Shuker, S. B., Hajduk, P. J., Meadows, R. P., and Fesik, S. W. (1996) Discovering high-affinity ligands for proteins: SAR by NMR. *Science 274*, 1531−1534.

(23) Petros, A. M., Huth, J. R., Oost, T., Park, C. M., Ding, H., Wang, X., Zhang, H., Nimmer, P., Mendoza, R., Sun, C., Mack, J., Walter, K., Dorwin, S., Gramling, E., Ladror, U., Rosenberg, S. H., Elmore, S. W., Fesik, S. W., and Hajduk, P. J. (2010) Discovery of a potent and selective Bcl-2 inhibitor using SAR by NMR. *Bioorg. Med. Chem. Lett. 20*, 6587−6591.

(24) Bochkareva, E., Kaustov, L., Ayed, A., Yi, G. S., Lu, Y., Pineda-Lucena, A., Liao, J. C., Okorokov, A. L., Milner, J., Arrowsmith, C. H., and Bochkarev, A. (2005) Single-stranded DNA mimicry in the p53 transactivation domain interaction with replication protein A. *Proc. Natl. Acad. Sci. U.S.A. 102*, 15412−15417.

(25) Souza-Fagundes, E. M., Frank, A. O., Feldkamp, M. D., Dorset, D. C., Chazin, W. J., Rossanese, O. W., Olejniczak, E. T., and Fesik, S. W. (2012) A high-throughput fluorescence polarization anisotropy assay for the 70N domain of replication protein A. *Anal. Biochem. 421*, 742−749.

(26) Otwinowski, Z., and Minor, W. (1997) Processing of X-ray Diffraction Data Collected in Oscillation Mode. *Methods Enzymol. 276*, 307−326.

(27) Winn, M. D., Ballard, C. C., Cowtan, K. D., Dodson, E. J., Emsley, P., Evans, P. R., Keegan, R. M., Krissinel, E. B., Leslie, A. G., McCoy, A., McNicholas, S. J., Murshudov, G. N., Pannu, N. S., Potterton, E. A., Powell, H. R., Read, R. J., Vagin, A., and Wilson, K. S. (2011) Overview of the CCP4 suite and current developments. *Acta Crystallogr. D67*, 235−242.

(28) Emsley, P., and Cowtan, K. (2004) Coot: Model-building tools for molecular graphics. *Acta Crystallogr. D60*, 2126−2132.

(29) Adams, P. D., Afonine, P. V., Bunkoczi, G., Chen, V. B., Davis, I. W., Echols, N., Headd, J. J., Hung, L. W., Kapral, G. J., Grosse-Kunstleve, R. W., McCoy, A. J., Moriarty, N. W., Oeffner, R., Read, R. J., Richardson, D. C., Richardson, J. S., Terwilliger, T. C., and Zwart, P. H. (2010) PHENIX: A comprehensive Python-based system for macromolecular structure solution. *Acta Crystallogr. D66*, 213−221.

(30) Baker, N. A., Sept, D., Joseph, S., Holst, M. J., and McCammon, J. A. (2001) Electrostatics of nanosystems: Application to microtubules and the ribosome. *Proc. Natl. Acad. Sci. U.S.A. 98*, 10037−10041.

(31) Delaglio, F., Grzesiek, S., Vuister, G. W., Zhu, G., Pfeifer, J., and Bax, A. (1995) NMRPipe: A multidimensional spectral processing system based on UNIX pipes. *J. Biomol. NMR 6*, 277−293.

(32) Hoffman, R. M., Li, M. X., and Sykes, B. D. (2005) The binding of W7, an inhibitor of striated muscle contraction, to cardiac troponin C. *Biochemistry 44*, 15750−15759.

(33) Muchmore, S. W., and Hajduk, P. J. (2003) Crystallography, NMR and virtual screening: Integrated tools for drug discovery. *Curr. Opin. Drug Discovery Dev. 6*, 544−549.

(34) Ruggiero, A., Smaldone, G., Squeglia, F., and Berisio, R. (2012) Enhanced crystallizability by protein engineering approaches: A general overview. *Protein Pept. Lett. 19*, 732−742.

(35) Derewenda, Z. S. (2011) It's all in the crystals. *Acta Crystallogr. D67*, 243−248.

(36) Bolanos-Garcia, V. M., and Chayen, N. E. (2009) New directions in conventional methods of protein crystallization. *Prog. Biophys. Mol. Biol. 101*, 3−12.

(37) Dale, G. E., Oefner, C., and D'Arcy, A. (2003) The protein as a variable in protein crystallization. *J. Struct. Biol. 142*, 88−97.

(38) Bauman, J. D., Das, K., Ho, W. C., Baweja, M., Himmel, D. M., Clark, A. D., Jr., Oren, D. A., Boyer, P. L., Hughes, S. H., Shatkin, A. J., and Arnold, E. (2008) Crystal engineering of HIV-1 reverse transcriptase for structure-based drug design. *Nucleic Acids Res. 36*, 5083−5092.

(39) Goldschmidt, L., Cooper, D. R., Derewenda, Z. S., and Eisenberg, D. (2007) Toward rational protein crystallization: A Web server for the design of crystallizable protein variants. *Protein Sci. 16*, 1569−1576.

(40) Horer, S., Reinert, D., Ostmann, K., Hoevels, Y., and Nar, H. (2013) Crystal-contact engineering to obtain a crystal form of the Kelch domain of human Keap1 suitable for ligand-soaking experiments. *Acta Crystallogr. F69*, 592−596.

(41) Moon, A. F., Mueller, G. A., Zhong, X., and Pedersen, L. C. (2010) A synergistic approach to protein crystallization: Combination of a fixed-arm carrier with surface entropy reduction. *Protein Sci. 19*, 901−913.

(42) Yamada, H., Tamada, T., Kosaka, M., Miyata, K., Fujiki, S., Tano, M., Moriya, M., Yamanishi, M., Honjo, E., Tada, H., Ino, T., Yamaguchi, H., Futami, J., Seno, M., Nomoto, T., Hirata, T., Yoshimura, M., and Kuroki, R. (2007) 'Crystal lattice engineering,' an approach to engineer protein crystal contacts by creating intermolecular symmetry: Crystallization and structure determination of a mutant human RNase 1 with a hydrophobic interface of leucines. *Protein Sci. 16*, 1389−1397.

(43) Derewenda, Z. S. (2004) Rational protein crystallization by mutational surface engineering. *Structure 12*, 529−535.